Draft version July 28, 2016
Preprint typeset using LaTeX style emulateapj v. 5/2/11

arXiv:1506.01107v2 [astro-ph.HE] 27 Jul 2016

RADIATIVE TRANSFER MODELS FOR GAMMA-RAY BURSTS

Indrek Vurm[1,2] and Andrei M. Beloborodov[1]
[1]Physics Department and Columbia Astrophysics Laboratory, Columbia University, 538 West 120th Street, New York, NY 10027, USA
[2]Tartu Observatory, Tõravere 61602, Tartumaa, Estonia

Draft version July 28, 2016

ABSTRACT

We present global radiative transfer models for heated relativistic jets. The simulations include all relevant radiative processes, starting deep in the opaque zone and following the evolution of radiation to and beyond the photosphere of the jet. The transfer models are compared with three gamma-ray bursts GRB 990123, GRB 090902B, and GRB 130427A, which have well-measured and different spectra. The models provide good fits to the observed spectra in all three cases, and we obtain estimates for the jet magnetization parameter $\varepsilon_{\rm B}$ and the Lorentz factor Γ. In the small sample of three bursts, $\varepsilon_{\rm B}$ varies between 0.01 and 0.05, and Γ varies between 400 and 1200.

Subject headings: gamma-ray burst: general – plasmas – radiation mechanisms: non-thermal – radiative transfer – scattering

1. INTRODUCTION

Cosmological gamma-ray bursts (GRBs) have been observed for more than four decades, and thousands of bursts have rather well measured spectra. No physical model has been demonstrated to systematically fit the observed spectra. Instead, the data are usually described using a phenomenological Band function (Band et al. 1993) or a Band function combined with a blackbody and a power law (Ryde & Pe'er 2009; Guiriec et al. 2015). The spectrum peaks at photon energy $E_{\rm pk}$ which is normally comparable to 1 MeV (Kaneko et al. 2006; Goldstein et al. 2012) and almost never exceeds 10 MeV.

1.1. *Transparent or opaque source?*

A simple interpretation of the observed nonthermal spectrum would be synchrotron emission from suddenly accelerated and quickly cooled electrons in an optically thin source. Then the MeV peak of the GRB spectrum comes from the peak of the electron energy distribution $n_{\rm e}(\gamma)$ and the gamma-ray tail comes from the high-energy tail in $n_{\rm e}(\gamma)$. This picture has to assume that the plasma has no dominant Maxwellian component. Fitting the prompt data with synchrotron models using a Maxwellian plus power-law electron distribution either requires the Maxwellian to be significantly weaker than the non-thermal component (Baring & Braby 2004; Burgess et al. 2011), or at most comparable in energy (Burgess et al. 2014). The peak of the GRB spectrum is then associated with a cutoff of the dominant non-thermal electron distribution at low energies. The origin of such a special distribution is unknown. Simulations of possible heating mechanisms — shocks and magnetic reconnection — give different $n_{\rm e}(\gamma)$. Shock heating results in a dominant Maxwellian component with only a small fraction of particles populating the high-energy tail (Sironi & Spitkovsky 2011), and reconnection gives a broad flat distribution with no cutoff at low energies (Kagan et al. 2015).

Regardless of the heating mechanism, the synchrotron model faces a problem when it is compared with observations. The synchrotron spectrum has a rather broad peak, even when the source is assumed to have a uniform magnetic field B and the power-law electron distribution is assumed to have a sharp cutoff at low energies. Attempts to reproduce GRB spectra with such idealized models gave acceptable fits for a small number of bursts (Baring & Braby 2004; Burgess et al. 2011, 2014; Preece et al. 2014). In a more realistic model, several factors inevitably broaden the synchrotron peak (Beloborodov 2013, hereafter B13), which makes it incompatible with observed spectra in virtually all GRBs (Axelsson & Borgonovo 2015; Yu et al. 2015).

This problem is illustrated in Figure 1 where a synchrotron spectrum is compared with the Band fit of a bright burst with a typical spectrum, GRB 990123. In the realistic fast-cooling regime, the minimum width of the synchrotron peak at half maximum exceeds 1.5 orders in photon energy, even with a single value of B in the emitting source and the narrow injected electron distribution (Maxwellian). It is significantly broader than the Band fit to the *time-average* of the variable GRB spectrum (Briggs et al. 1999). Uncertainties in the observed spectrum due to the detector response and limited photon statistics allow some room for stretching the measured peak width, however can hardly be made consistent with the synchrotron model, especially when the inevitable broadening due to variable magnetic field, electron injection, and Doppler factor is taken into account.

The sharp MeV spectral peak provides strong evidence for thermalization of radiation at early, opaque stages of the GRB explosion. The inheritance of the spectral peak from an initial thermalization stage is also supported by the observed distribution of $E_{\rm pk}$, which cuts off above ~ 10 MeV in agreement with a theoretical maximum (B13). In addition, many GRBs show hard spectral slopes violating the "line of death" for optically thin synchrotron emission (Preece et al. 2000; Kaneko et al. 2006) and suggesting an opaque source.

Accepting that the MeV peak of GRB spectrum forms inside an opaque jet leads to so-called "photospheric" emission models. The burst radiation is released where the jet becomes sufficiently transparent to scattering, and

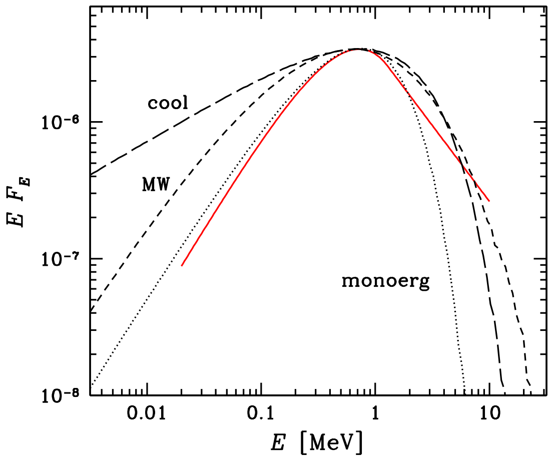

Figure 1. Synchrotron spectra from an optically thin spherical shell with three electron distributions: mono-energetic (dotted line), Maxwellian (short-dashed line), and fast-cooling Maxwellian (long-dashed line). For comparison the Band fit of GRB 990123 is shown by the red thick curve.

its spectrum is mainly shaped by subphotospheric radiative processes. Several versions of the photospheric model have been proposed over the years (Thompson 1994; Eichler & Levinson 2000; Mészáros & Rees 2000; Giannios & Spruit 2007; Beloborodov 2010, hereafter B10; Levinson 2012; Thompson & Gill 2014). All share a key feature: the jet is *dissipative*, i.e. significantly heated as it propagates away from the central engine. This heating modifies the emitted photospheric radiation from simple blackbody emission. The resulting spectrum was shown to have a nonthermal shape that closely resembles the phenomenological Band function (Pe'er et al. 2006; Giannios 2008; B10; Vurm et al. 2011, hereafter V11). It was proposed that the dissipative photosphere model provides a good description to the observed spectra (Ryde et al. 2011) and needs to be carefully tested against observations.

1.2. *Internal dissipation*

Four dissipation mechanisms have been proposed as sources of GRB emission: collisionless shocks (Rees & Meszaros 1994), damping of Alfvén wave turbulence (Thompson 1994), magnetic reconnection (Drenkhahn & Spruit 2002), and neutron collisions (B10). Magnetic field and internal bulk motions provide the energy reservoirs available for dissipation.

The presence of strong internal motions in the jet is indicated by the observed variability of GRB radiation. The central engine of the explosion is likely unsteady, and additional variability is induced as the jet burrows its way through the progenitor star and the cocoon produced by the jet-star interaction (Lazzati et al. 2009). This leads to multiple internal and recollimation shocks, which keep the jet hot and relatively slow when it emerges from the stellar progenitor. Thus, shock heating is expected to occur in an extended range of radii and in an extended range of timescales, which is consistent with the observed broad power spectrum of variability (Beloborodov et al. 2000; Morsony et al. 2010).

Additional evidence for dissipation at small radii is provided by the observed *photon number* emitted in GRBs. In many GRBs, the central engine is unable to provide the observed photons, so additional photons must be produced in the expanding jet. Photon production is a direct consequence of dissipation at large optical depths (B13; Vurm et al. 2013, hereafter V13; see also Eichler & Levinson 2000; Thompson et al. 2007). Observations also require that dissipation continues at least to the photospheric radius, so that the released spectrum has a nonthermal shape. Therefore, in this paper we consider outflows which remain dissipative across a broad range of distances from the central engine, starting from the region inside the progenitor and extending to the jet photosphere and beyond.

As long as baryons dominate the plasma inertia, dissipation of internal motions may be expected to heat the ions (and neutrons) in the first place. Efficient dissipation should give a typical energy of ~ 1 GeV per nucleon (its rest mass) in a relativistic jet. Baryons themselves do not emit significant radiation, because of their large mass-to-charge ratio, however their energy can be passed to the electrons and radiated in the following ways:

1. Coulomb collisions gradually pass energy from the hot ions to the thermalized electron/positron population (which is kept much colder by efficient radiative cooling).

2. Inelastic (pion-producing) nuclear collisions generate a non-thermal $e^{\pm}$ population with Lorentz factor $\gamma_{\rm inj} \sim m_\pi/m_e \sim 300$.

3. Plasma motion through a radiation-mediated shock has a steep velocity gradient, leading to bulk Comptonization of photons by the electrons. Bulk Comptonization could also result from plasma turbulence on small scales.

4. Collective plasma processes in a collisionless shock suddenly heat the electrons to an ultra-relativistic temperature.

All these processes are important in sub-photospheric internal shocks (Beloborodov 2016). Electrons can also be directly heated by magnetic reconnection, tapping into the magnetic energy carried by the jet.

1.3. *Evolution of radiation in the expanding jet*

The energized electrons rapidly lose their energy to radiation via inverse Compton (IC) scattering, synchrotron emission, and (at extremely high optical depths) through double Compton scattering and bremsstrahlung. The produced photons are redistributed in energy by Compton scattering and form the spectrum that eventually escapes at the Thomson photosphere $R_\star$ where the scattering optical depth $\tau_{\rm T}$ drops below unity.

Three relevant regions in the jet were described in B13:

1. The Planck zone ($r \lesssim 10^{10}$ cm, $\tau_{\rm T} \gtrsim 10^5$): the density of the jet is sufficiently high to maintain blackbody radiation in detailed equilibrium with the thermalized plasma.

2. The Wien zone ($\tau_{\rm T} \gtrsim 10^2$): the dissipated heat is thermalized into a Bose-Einstein photon distribution with a *finite chemical potential.* The number of photons accumulated in the Wien peak attains its final value near the Wien radius, beyond which Comptonization is unable to bring new generated photons to the spectral peak.

3. Unsaturated Comptonization zone ($\tau_{\rm T} \lesssim 10^2$): heating maintains a Compton parameter $y \sim 1$. The final non-thermal shape of the spectrum is produced in this region.

The GRB radiation emerging at the photosphere carries information about the entire expansion history of the jet. Thus, the observed spectrum may be used to reconstruct dissipative processes hidden in the opaque region behind the photosphere.

It is best to view the formation of the observed spectrum as a problem of radiative transfer in an ultra-relativistic outflow (Beloborodov 2011, hereafter B11). The problem must be solved consistently with the flow dynamics and heating. Boundary conditions should be set sufficiently close to the central engine where the hot and dense plasma is capable of producing and thermalizing photons, so that these processes can be explicitly followed by the transfer simulation. Radiative transfer from the inner region to and beyond the photosphere determines the radiation spectrum released by the jet.

1.4. *This paper*

Our main goal in this paper is the development of a global radiative transfer model for heated jets and the application of the model to observed GRBs. The main novel feature of our simulations is the explicit inclusion of photon production reactions in the transfer problem. This requires one to start the simulation at a small radius, extremely deep below the photosphere.

This paper focuses on jets whose energy is dominated by matter and radiation, and a modest magnetization parameter $\varepsilon_{\rm B} < 1$ is assumed. We defer our study of magnetically-dominated jets to a future work; a recent discussion of radiative processes in magnetically dominated jets is found in Gill & Thompson (2014); Thompson & Gill (2014) and Bégué & Pe'er (2015).

To keep the number of parameters to a minimum we employ a simple model of continuous internal dissipation approximating the average heating rates (thermal and non-thermal) as power laws of radius. This may be a crude approximation to jet heating by multiple internal shocks or reconnection, however it allows us to study the global picture of the evolution of radiative processes with radius. As will be demonstrated below, the formation of photospheric radiation extends over several decades in radius, and the transfer simulation allows us to study all stages of this process. The small number of parameters in the model makes it useful for fitting the data.

The simulations presented in this paper are performed with an improved version of the kinetic code developed by Vurm & Poutanen (2009) and Vurm et al. (2011). It follows in detail all relevant radiative processes expected in a heated jet, thermal and nonthermal. The thermal processes include Comptonization of photons by the thermal plasma, induced Compton scattering at low frequencies, cyclotron emission/absorption, bremsstrahlung, and double Compton scattering. The rates of all these processes are well defined and accurately calculated for a given density, temperature, and magnetic field.

The injection of relativistic leptons by nuclear collisions or by collisionless heating (Beloborodov 2016) leads to synchrotron emission inside the jet, which is an important source of photons. Relativistic leptons also generate an IC $e^{\pm}$ cascade; it is calculated in detail using exact cross sections. The density of $e^{\pm}$ pairs is governed by the rates of their creation and annihilation; accurate calculation of $e^{\pm}$ density is essential as it can strongly dominate over the electron-ion plasma density.

The paper is organized as follows. Section 2 describes the setup of the transfer problem and the physical processes involved. Sample models are presented in Section 3 where we explore how the emitted spectrum is formed as the jet expands over several decades in radius, how the emerging radiation is influenced by the jet magnetization, acceleration history etc. In Section 4, we apply the model to three bright bursts with high-quality spectral data: GRB 990123, GRB 090902B and GRB 130427A. The results are discussed in Section 5.

2. SETUP OF THE TRANSFER SIMULATION

2.1. *Dynamics of the jet*

We assume that the jet collimation occurs inside a characteristic radius $R_{\rm c}$ and its subsequent expansion at $r > R_{\rm c}$ may be approximated as conical. In our models, $R_{\rm c}$ is typically chosen around 10^{11} cm; our simulations start at this radius. The jet is still accelerating at this stage, and its Lorentz factor saturates at a much larger radius; the acceleration is self-consistently calculated as described below.

The jet variability is viewed as internal turbulent motions $\Delta\Gamma$ superimposed on a steady flow with Lorentz factor $\Gamma(r)$. At any radius r, the internal motions can be divided into two parts: large-scale "frozen" fluctuations (length-scale larger than the local "horizon" — the size of the casually connected region) and small-scale evolving fluctuations. This decomposition is similar to the analysis of primordial perturbations in cosmology. The small-scale fluctuations are dissipative, and they are assumed in our radiative transfer problem to be the source of heat and nonthermal particles. The jet heating must be unsteady; however, we simplify the simulation by using a smoothed, averaged heating rate. When calculating radiative transfer, we average out $\Delta\Gamma$ and view Γ as a single-valued function of radius r (or the comoving time of the steady background flow). Then radiative transfer can be modeled in a steady-state approximation, which significantly simplifies the calculations (see B11 for discussion of this approximation).

The turbulent motions $\Delta\Gamma$ are only viewed as a reservoir of energy available for dissipation. Then the total jet luminosity may be decomposed as

$$L = L_{\rm pl} + L_{\rm rad} + L_B + L_{\rm turb} = const. \qquad (1)$$

Here $L_{\rm pl}(r)$ is the steady component of the plasma energy flow rate separated from the turbulent component $L_{\rm turb}(r)$ (the reservoir); $L_{\rm rad}(r)$ and $L_B(r)$ are the energy flows carried by radiation and magnetic field. As the jet propagates, energy can be redistributed between the different components in Equation (1). The dissipated part of the turbulence reservoir gets converted to the plasma internal energy, which is immediately transferred to radiation via rapid cooling; thus effectively there is a gradual transformation $L_{\rm turb} \to L_{\rm rad}$. In the simulations presented below, we keep L_B = constant for simplicity; in reality, the magnetic component may have a 'reducible' component available for dissipation, e.g. via reconnection. However, when $\varepsilon_{\rm B} = L_B/L \ll 1$ the dissipation of magnetic fields cannot serve as the main source of GRB radiation.

Radiation can efficiently accelerate the jet at early stages, when it dominates the jet energy. Thus we also expect the gradual transformation $L_{\rm rad} \to L_{\rm pl}$. The dynamical equation for the jet Lorentz factor Γ is given by (see B11),

$$\frac{d\Gamma}{dr} = \sigma_{\rm T} Z_\pm \frac{4\pi I_1}{m_p c^3}, \tag{2}$$

where $4\pi I_1$ is the radiation flux measured in the rest-frame of the jet (I_1 is the first moment of the local radiation intensity), and $Z_\pm$ is the number of electrons and positrons per proton. Equation (2) assumes $L_{\rm pl} \approx \Gamma \dot{M} c^2$; this is a good approximation as long as the ion temperature is non-relativistic.

We use Equation (2) in our simulations to calculate the self-consistent $\Gamma(r)$. At very large optical depths, where radiation is nearly isotropic and I_1 is small, an alternative form of the dynamical equation can be used, which does not depend explicitly on I_1, see Equation (A13) in Appendix A.

2.2. *Kinetic equations*

At optical depths $\tau_{\rm T} \gtrsim 100$ the radiation field is nearly isotropic in the jet rest frame, and the bulk of leptons are kept at a non-relativistic temperature. The evolution of radiation under such conditions is well described by the Kompaneets equation. For a conical accelerating outflow it takes the form

$$\frac{1}{r^2\Gamma}\frac{\partial}{\partial \ln r}\left(r^2\Gamma\,\tilde{n}\right) = \frac{r}{c\Gamma}(\tilde{j}_\nu - c\kappa_\nu \tilde{n}) + \frac{1}{x^2}\frac{\partial}{\partial x}\left[\tau_{\rm T} x^4\left(\theta_{\rm e}\frac{\partial \tilde{n}}{\partial x} + \tilde{n} + \tilde{n}^2\right) + \frac{3-g}{3}\,x^3\tilde{n}\right], \tag{3}$$

where $\tilde{n}$ is the photon occupation number, $x = h\nu/m_{\rm e}c^2$ is the dimensionless photon energy and $\theta_{\rm e} = k_{\rm B}T_{\rm e}/m_{\rm e}c^2$ is the dimensionless electron temperature. The last term in square brackets accounts for adiabatic cooling of radiation, where

$$g = 1 - \frac{d\ln\Gamma}{d\ln r}. \tag{4}$$

All quantities except r and Γ are measured in the instantaneous comoving frame of the jet. The opacity κ_ν and the source term $\tilde{j}_\nu$ account for all relevant radiative processes (see Section 2.3) except thermal Comptonization, which is described by the Kompaneets equation itself. Note that it is essential to include the induced $\tilde{n}^2$ term in the Kompaneets equation to accurately account for the number of synchrotron photons that can be upscattered to the Wien peak (V13); neglecting this term would lead to an overestimation of the photon number in the Wien peak.

The deviation from isotropy develops at optical depths $\tau_{\rm T} \sim$ a few tens (B11), roughly near the Wien radius. At larger radii one has to solve the full angle-dependent radiative transfer equation (Mihalas 1980; B11),[1]

$$\frac{1}{r^2\Gamma}\frac{\partial}{\partial \ln r}\left[(1+\mu)r^2\Gamma I_\nu\right] = \frac{r}{\Gamma}(j_\nu - \kappa_\nu I_\nu) + (1+\mu)(1-g\mu)\frac{\partial I_\nu}{\partial \ln \nu} - \frac{\partial}{\partial \mu}\left[(1-\mu^2)(1+\mu)\,gI_\nu\right], \tag{5}$$

where I_ν is the comoving specific intensity, $\mu = \cos\theta$, θ is the (comoving frame) angle relative to the radial direction, and j_ν is the emissivity. This equation accurately describes the relativistic radiative transfer in three dimensions for spherically symmetric outflows with $\Gamma \gtrsim 10$.

The evolution of the electron/positron distribution is described by the kinetic equation

$$\frac{1}{r^2\Gamma}\frac{\partial}{\partial \ln r}\left[r^2\Gamma\, n_\pm(p)\right] = \frac{r}{c\Gamma}(j_\pm - c\kappa_\pm n_\pm(p)) - \frac{\partial}{\partial p}\left\{\frac{r}{c\Gamma}\left[\dot{p}\, n_\pm(p) - \frac{1}{2}\frac{\partial}{\partial \gamma}\left[D n_\pm(p)\right]\right] - \frac{3-g}{3}\,p\, n_\pm(p)\right\}, \tag{6}$$

where $p = \sqrt{\gamma^2-1}$ is the electron/positron momentum in units of $m_e c$, and $n_\pm(p)$ is the electron/positron density per unit momentum interval. The terms $\dot{p}$ and D account for heating/cooling and diffusion in momentum space due to radiative processes and Coulomb collisions. The emission term $j_\pm$ includes the injection of new pairs due to non-thermal dissipation and photon-photon absorption $\gamma + \gamma \to e^+ + e^-$, and $c\kappa_\pm n_\pm(p)$ is the pair annihilation rate. All these terms are accurately calculated as described in Vurm & Poutanen (2009) and Vurm et al. (2011). The last term in curly brackets describes adiabatic cooling.

In the simulation the photon equation is solved together with the kinetic equations for electrons/positrons and the dynamical equation (2) for $\Gamma(r)$. The photon and lepton equations are coupled via the interaction terms $\tilde{j}_\nu$ (j_ν), κ_ν, $j_\pm$, $\kappa_\pm$, $\dot{p}$ and D. The switch from the Kompaneets equation (3) to the radiative transfer equation (5) is made at $\tau_{\rm T} = 100$; at this stage either of these equations is sufficiently accurate, allowing for a smooth transition. The evolution is followed to $\tau_{\rm T} \ll 1$. The simulation is typically stopped at $\tau_{\rm T} \lesssim 0.1$ where the obtained radiation field is transformed to the observer frame and assumed to escape.

2.3. *Radiative processes and photon generation*

Radiative processes in the expanding jet determine the observed GRB spectrum and require accurate calculations at all radii, including very opaque regions far below the photosphere. In particular, the position of the spectral peak is controlled by photon generation below the Wien radius, where photons are produced at low energies and up-scattered to the peak via saturated Comptonization. The photon generation mechanisms can be categorized a follows (B13, V13):

---

[1] In contrast to the Kompaneets equation, Equation (5) neglects induced downscattering, which affects the rate of photon upscattering from low energies toward the Wien peak. This loss of accuracy is acceptable, because our simulation switches to Equation (5) outside the Wien zone where upscattering has stopped populating the Wien peak with new photons.

1. Thermal: photons are generated by Maxwellian leptons. Thermal radiative processes operate efficiently only in the Planck zone ($\tau_{\rm T} \gtrsim 10^5$). These processes include double Compton scattering, bremsstrahlung (less efficient than double Compton unless the jet is strongly clumped), and cyclotron emission. The efficiency of cyclotron emission can be similar to that of double Compton scattering if the jet is strongly magnetized.

2. Nonthermal: photons are generated by relativistic nonthermal electrons/positrons. The main radiative process is synchrotron emission. It continues to operate outside the Planck zone, and the number of produced photons typically *increases* with radius, as long as the non-thermal dissipation channel remains active.

The rates of the thermal processes are given in B13 and V13. The implementation of nonthermal synchrotron emission is similar to that in V13, with one significant extension: we are considering jets with moderate magnetization $\varepsilon_{\rm B} \sim 10^{-3} - 10^{-1}$ where pair-photon cascades produce a larger number of secondary nonthermal particles (see below). In contrast, V13 considered magnetizations close to equipartition where pair cascades are suppressed.

2.4. *Heating rate*

The total (thermal and non-thermal) heating rate satisfies

$$\frac{dL_{\rm h}}{d\ln r} \equiv \frac{dL_{\rm th}}{d\ln r} + \frac{dL_{\rm nth}}{d\ln r} = -\frac{dL_{\rm turb}}{d\ln r}. \quad (7)$$

The simulations presented below assume that the fractional luminosities dissipated via the thermal and nonthermal channels follow a power law,

$$\varepsilon_{\rm th} \equiv \frac{1}{L}\frac{dL_{\rm th}}{d\ln r} = \varepsilon_{0,\rm th}\left(\frac{r}{R_{\rm c}}\right)^{k_{\rm th}}, \quad (8)$$

$$\varepsilon_{\rm nth} \equiv \frac{1}{L}\frac{dL_{\rm nth}}{d\ln r} = \varepsilon_{0,\rm nth}\left(\frac{r}{R_{\rm c}}\right)^{k_{\rm nth}}. \quad (9)$$

The corresponding heating and injection rates in Equation (6) are

$$\dot{p}_{\rm h} = \frac{\gamma}{p}\dot{\gamma}_{\rm h} = \frac{\gamma}{p}\frac{\varepsilon_{\rm th} L}{4\pi m_{\rm e} c^2 r^3 \Gamma (n_- + n_+)}, \quad (10)$$

and

$$j_{\pm,\rm inj} = \frac{\varepsilon_{\rm nth} L}{4\pi m_{\rm e} c^2 r^3 \Gamma}\,\frac{\delta(p - p_{\rm inj})}{2\gamma_{\rm inj}}, \quad (11)$$

where n_- and n_+ are the electron and positron densities, respectively, $p_{\rm inj}$ is the dimensionless momentum of the injected pairs, and $\gamma_{\rm inj} = (1 + p_{\rm inj}^2)^{1/2}$ is their Lorentz factor.

2.5. *Parameters of the model*

The GRB models presented below have the following set of parameters:

(1) Total jet luminosity L (isotropic equivalent).
(2) Energy per baryon $\eta = L/\dot{M}c^2$.
(3) Magnetization $\varepsilon_{\rm B} = L_B/L$.
(4) The jet Lorentz factor at the radius $R_{\rm c}$ where the simulation starts; $R_{\rm c}$ is chosen near the radius of the jet breakout from the progenitor star.
(5) The jet energy per photon, i.e. the initial $E_{\rm pk}$. In our models the jet is initially photon starved, i.e. we choose a high $E_{\rm pk} \approx 10$ MeV. This is done to demonstrate that even in weakly magnetized jets synchrotron emission can efficiently produce photons. Then the predicted GRB spectrum weakly depends on the choice of initial $E_{\rm pk}$.
(6) The efficiencies of thermal and nonthermal heating, $\varepsilon_{\rm th}$ and $\varepsilon_{\rm nth}$. In most of our models heating is assumed to have a flat distribution over $\ln r$ ($k_{\rm th} = k_{\rm nth} = 0$ in Equations (8) and (9)); we will also consider a few variations in the heating history of the jet if this is required to fit the observed GRB spectra.

The non-thermal lepton injection energy is fixed at $\gamma_{\rm inj} = 300 \approx m_\pi/m_e$, as expected for collisional heating; its exact value weakly affects the results.

3. SAMPLE MODELS

3.1. *Overview of the spectral evolution*

Figure 2 illustrates the evolution of the photon spectrum within a dissipative jet as the radiation is carried from highly opaque regions to transparency. There are two main stages of the spectral evolution:

(1) Generation of photons below the Wien radius ($\tau_{\rm T} \gtrsim 10^2$) and their Comptonization to the Wien peak. The growth of photon number in the Wien peak results in its shift to lower energies. The high-energy tail is suppressed at $r < R_{\rm W}$ for two reasons. First, the electrons are kept approximately at the Compton temperature, i.e. $3k_{\rm B}T_{\rm e} \approx E_{\rm pk}/\Gamma$. Thus thermal Comptonization is hardly capable of populating the photon spectrum above $E_{\rm pk}$, leading to an exponential cutoff at $E_{\rm pk}$. Secondly, the nonthermal radiation from IC scattering by relativistic pairs does not survive at $\tau_{\rm T} \gg 1$ — it is reprocessed to lower energies via the pair-photon cascade and downscattering by the thermal pairs.

(2) Broadening of the spectrum by unsaturated Comptonization outside the Wien radius, leading to a nonthermal shape of the spectrum. The broadening first affects the low-energy slope α, which begins to soften near the Wien radius and attains its final value near the photosphere. The resulting photon index $\alpha \sim -1$ depends on the heating history at $r > R_{\rm W}$, in particular on the nonthermal dissipation channel, as the unsaturated Comptonization of the fresh low-energy synchrotron photons governs the softening of α. Without nonthermal dissipation the low-energy spectral slope would be much harder.

The photospheric spectrum also broadens at high energies. The high-energy tail is mostly built around and above the photosphere, due to two effects, thermal and nonthermal. Outside the Wien radius the electron temperature rises significantly above $E_{\rm pk}/\Gamma$ (see below) and thermal Comptonization begins to produce photons with energies $E > E_{\rm pk}$. As the optical depth drops, the

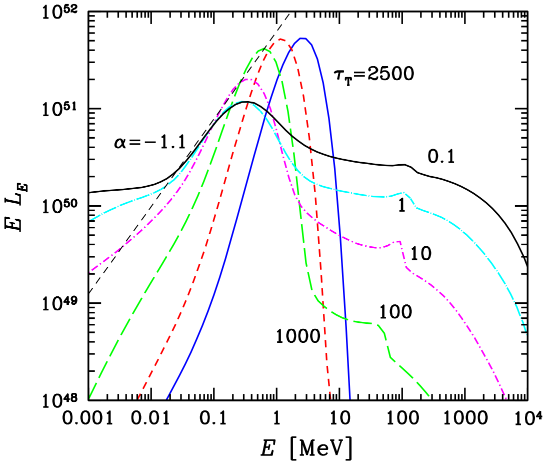

Figure 2. Evolution of the radiation spectrum carried by the jet, from high to low optical depths $\tau_{\rm T}$. This sample model has the following parameters: $L = 2 \times 10^{52}$ erg/s, $\eta = 190$, $R_{\rm c} = 10^{11}$ cm, $\gamma_0 = 300$, $\varepsilon_{\rm th} + \varepsilon_{\rm nth} = 0.05$, $\varepsilon_{\rm th}/\varepsilon_{\rm nth} = 1$, $\Gamma(R_{\rm c}) = 20$, magnetization $\varepsilon_{\rm B} = 10^{-2}$. The spectra are measured in the rest frame of the central engine and not corrected for a cosmological redshift.

nonthermal high-energy component becomes increasingly prominent, especially in weakly magnetized jets. Then the overlapping thermal and nonthermal Comptonization components together form an extended high-energy spectrum which can easily be mistaken for a single emission component (see also B10; V11). In contrast, in strongly magnetized jets with $\varepsilon_{\rm B} \sim 1$, the pair cascade and nonthermal Comptonization are reduced, leading to a different spectral shape at high energies (see Figure 5 in V11).

It is worth noting that the overall spectrum has a distinctly nonthermal shape already well below the photosphere (at $\tau_{\rm T} \gtrsim 10$). In particular, the low-energy slope is significantly softer than the Planck (or Wien) spectrum. Even if dissipation stopped completely at $\tau_{\rm T} \sim 10$, a thermal-looking prompt emission would not be expected; instead, the emerging spectrum would resemble a cutoff power law.

A thermal-looking GRB spectrum would only be produced in a special case when all dissipation is confined to very high optical depths. Even in this case, however, the transfer effects would soften α from the thermal slope to $\alpha \sim 0.4$ (B10; see also Pe'er & Ryde 2011).

3.2. $e^{\pm}$ *cascade and pair loading*

When the jet magnetization is weak, $\varepsilon_{\rm B} < 0.1$, the relativistic $e^{\pm}$ pairs injected by the nonthermal dissipation channel lose their energy primarily through IC scattering of photons from the quasi-thermal (Wien) peak. The upscattered photons with energies above $m_{\rm e}c^2$ in the jet frame immediately convert to secondary $e^{\pm}$ pairs through photon-photon collisions. The created particles also upscatter photons etc., leading to a pair-photon cascade that populates the jet with secondary $e^{\pm}$ pairs which can dominate the plasma.

The distribution of non-thermal leptons resulting from the cascade can be expressed as (cf. Equations (18) and (19) in V11)

$$n_{\rm e}(\gamma) = \frac{3Y\gamma_{\pm,\rm min}^{\alpha_\pm}}{4c\sigma_{\rm T}} \frac{\varepsilon_{\rm nth}}{(\varepsilon_{\rm B} + \varepsilon_{\rm rad})} \frac{c\Gamma}{r}\, \gamma^{-(\alpha_\pm + 2)}, \tag{12}$$

where $\varepsilon_{\rm B} = L^{-1} dL_B/d\ln r$, $\varepsilon_{\rm rad} = L^{-1} dL_{\rm rad}/d\ln r$, and $Y \sim 0.1$ is the pair yield (Svensson 1987). The saturated cascade turns off at $\gamma_{\pm,\rm min} \approx (m_{\rm e}c^2\Gamma/E_{\rm pk})^{1/2} \sim 10$; electrons at $\gamma < \gamma_{\pm,\rm min}$ are unable to upscatter photons from the Wien peak to MeV energies for further pair generation. The pair yield of the cascade generated by a primary particle with Lorentz factor $\gamma_{\rm inj}$ may be expressed as $Y = \mathcal{M}_{\rm s}/\gamma_{\rm inj}$, where $\mathcal{M}_{\rm s}$ is the pair multiplicity, i.e. the number of secondary $e^{\pm}$ per primary particle. The power-law index $\alpha_\pm \approx \ln \mathcal{M}_{\rm s}/(\ln\gamma_{\rm inj} - \ln\gamma_{\pm,\rm min})$ characterizes the additional steepening effect of the $e^{\pm}$ cascade on the standard cooling distribution $n_{\rm e}(\gamma) \propto \gamma^{-2}$.

Below the photosphere the pairs are in creation-annihilation equilibrium. Their density can be expressed as

$$n_{\rm e} = Z_\pm n_{\rm p}, \tag{13}$$

where the proton density is

$$n_{\rm p} = \frac{\dot{M}}{4\pi m_{\rm p} c\, r^2 \Gamma}, \tag{14}$$

and the pair loading factor $Z_\pm$ is given by (Appendix B; see also B10; Thompson & Gill 2014)

$$Z_\pm = \left(\frac{16\, Y \varepsilon_{\rm nth} L}{3\, \tau_{\rm p}\, \Gamma \dot{M} c^2} \frac{m_{\rm p}}{m_{\rm e}} + 1 \right)^{1/2} \propto (r\Gamma)^{1/2}. \tag{15}$$

The last proportionality is valid if $Z_\pm \gg 1$, i.e. if pairs dominate over the electron-ion plasma. This condition is met when the Thomson optical depth associated with n_p is sufficiently low,

$$\tau_{\rm p} = \frac{\sigma_{\rm T} n_{\rm p}\, r}{\Gamma} \ll \frac{16}{3} \frac{m_{\rm p}}{m_{\rm e}} \frac{Y \varepsilon_{\rm nth} L}{\Gamma \dot{M} c^2}. \tag{16}$$

This condition may not be satisfied in a region deep below the photosphere. The expanding jet becomes increasingly pair dominated in the subphotospheric region, provided that the nonthermal dissipation channel is active (Figure 3).

Pair annihilation freezes out when the annihilation time, $t_{\rm ann} = 16/(3c\sigma_{\rm T} n_\pm)$, exceeds the expansion time $t_{\rm dyn} = r/(c\Gamma)$, which occurs at $\tau_\pm = 16/3$. The pair-loading factor at this time is

$$Z_\pm = \frac{m_{\rm p}}{m_{\rm e}} \frac{\varepsilon_{\rm nth} Y L}{\Gamma \dot{M} c^2}, \tag{17}$$

where Γ, $\varepsilon_{\rm nth}$ and Y are taken at the freezeout radius. Typically, we find $Z_\pm \sim 10$ for moderate nonthermal injection rate $\varepsilon_{\rm nth} \sim 0.1$. As shown in Appendix B and seen in Figure 3, pair creation beyond the freezeout radius can increase $Z_\pm$ by a modest factor (at most logarithmically in r).

The pair loading increases the photospheric radius by the factor of $Z_\pm$ compared to the pair-free jet. Pair loading is significantly reduced if the jet magnetization $\varepsilon_{\rm B}$ is above a few percent, since synchrotron cooling becomes competitive with Compton cooling, inhibiting the pair-photon cascade and lowering Y (V11).

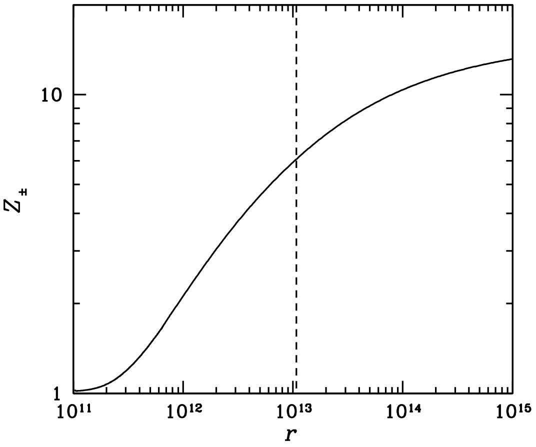

Figure 3. Evolution of pair-loading with radius in the simulation shown in Figure 2. The vertical dashed line indicates the freeze-out radius where $\tau_\pm = 16/3$.

3.3. *Building up the photon number in the Wien peak via synchrotron emission*

A fraction of the non-thermal lepton energy is converted to low-energy synchrotron radiation. If the magnetization is weak, this fraction is small, as the synchrotron losses of high-energy particles are small compared to their IC losses. While the energy budget of synchrotron radiation is small, the *number* of generated synchrotron photons is substantial, because of their low energies. Furthermore, these soft photons can gain energy from the thermal plasma through Comptonization. Below the Wien radius $R_{\rm W}$ many of them are Comptonized to the Wien peak and eventually dominate the peak, significantly increasing its photon number and shifting $E_{\rm pk}$ to lower energies. This shift is required by energy conservation (energy is shared between more photons) and accomplished through Compton cooling of the thermal plasma by the synchrotron photons.

The number of synchrotron photons that can be upscattered to the Wien peak depends on the competition of Compton upscattering against synchrotron reabsorption and induced Compton downscattering (V13). This competition defines a critical photon energy E_0 (and a corresponding $e^\pm$ Lorentz factor γ_0), above which upscattering dominates over other processes. The calculation of γ_0, E_0, and the number of synchrotron photons emitted above E_0 is given in Appendix C.

At $r < R_{\rm W}$ all synchrotron photons emitted at $E > E_0$ end up in the Wien peak. Most of them are emitted near E_0 by leptons with Lorentz factors $\gamma \sim \gamma_0$ (the emissivity scales as $E^{(-p+1)/2}$, where $p \geq 2$). Therefore, the rate at which photons are accumulated in the peak [cm^{-3} s^{-1}] is roughly proportional to the number of leptons with $\gamma \sim \gamma_0$,

$$\dot{\mathcal{N}}_{\rm synch} \approx \frac{\sigma_{\rm T} m_{\rm e} c^2 B}{3eh}\, \gamma_0 n_{\rm e}(\gamma_0). \tag{18}$$

The number of photons accumulated in the Wien peak is finalized near $R_{\rm W}$. The resulting flow of photon number through the sphere $4\pi R_{\rm W}^2$ (isotropic equivalent) is given by

$$\dot{N}_{\rm ph} = \int^{R_{\rm W}} 4\pi r^3\, \dot{\mathcal{N}}_{\rm synch}(r)\, d\ln r. \tag{19}$$

The photon number carried in the spectral peak is weakly changed outside the Wien radius; this number is eventually released at the photosphere.

The secondary $e^\pm$ pairs affect photon production by increasing both $n_{\rm e}$ and γ_0; the net effect is positive, i.e. the pair cascade enhances photon generation. Pair loading also increases $R_{\rm W}$ by increasing the flow opacity; this allows a longer time for the accumulation of photons in the Wien peak.

In contrast to thermal bremsstrahlung or double Compton effect, the synchrotron photon production increases with radius and the integral in Equation (19) peaks near $R_{\rm W}$. This behavior was seen for pair-free outflows in V13 and remains true in the presence of pair cascades (see Appendix C for analytical estimates). Our numerical simulations confirm that a substantial fraction of the photons accumulated in the spectral peak originates near the outer boundary of the Wien zone. This can be seen in Figure 2: the decrease of $E_{\rm pk}$ due to continuing photon supply to the peak ends around $\tau_{\rm T} \lesssim 100$, which approximately corresponds to $R_{\rm W}$.

As long as the nonthermal dissipation channel remains active, the production of synchrotron photons continues beyond the Wien radius. This results in the soft "excess" seen below a few×10 keV in the emitted spectrum (Figure 2, see also V11). More importantly, unsaturated Comptonization of these photons plays a key role in determining the spectral slope below the peak, which is discussed below.

3.4. *Comptonization*

The saturated Comptonization at $r < R_{\rm W}$ maintains a quasi-equilibrium between radiation and thermal plasma. The photon spectrum around the peak has a Wien shape, with small excesses at lower and higher energies due to synchrotron and non-thermal IC emission, respectively. At $r > R_{\rm W}$, the thermal Comptonization gradually switches to the unsaturated regime, where the Compton y-parameter remains close to unity, as long as the heating operates.

The y-parameter may be evaluated by considering the evolution of the radiation luminosity at $\tau_{\rm T} \gg 1$ (see Appendix A),

$$\frac{dL_{\rm rad}}{d\ln r} = -\frac{2g}{3} L_{\rm rad} + \frac{4}{3}\frac{dL_{\rm h}}{d\ln r}, \tag{20}$$

where the first and second terms on the right hand side account for adiabatic cooling and dissipation, respectively. Assuming $g = 1 - d\ln\Gamma/d\ln r \approx$ const and the scaling

$$\frac{dL_{\rm h}}{d\ln r} \propto r^{k_{\rm h}}, \tag{21}$$

one can solve Equation (20) for $L_{\rm rad}$,

$$L_{\rm rad} = \frac{4}{3k_{\rm h} + 2g}\,\frac{dL_{\rm h}}{d\ln r}. \tag{22}$$

The (thermal) heating of electrons is balanced by Compton losses,

$$\frac{dL_{\rm h}}{d\ln r} = \frac{3}{4}(y - y_{\rm C})L_{\rm rad}, \tag{23}$$

where $y = 4\tau_{\rm T}\theta_{\rm e}$ and $y_{\rm C} = 4\tau_{\rm T}\theta_{\rm C}$ are the Compton parameters corresponding to the electron and Compton temperatures, respectively. Substituting the solution (22) into the heating-cooling balance (23), one finds that the Compton parameter relaxes to

$$y - y_{\rm C} = k_{\rm h} + \frac{2g}{3}. \tag{24}$$

Thus $y - y_{\rm C}$ remains close to unity if the heating rate does not decline significantly faster than $dL_{\rm h}/d\ln r \propto r^0$. At the Wien radius $y \approx y_{\rm C} \approx$ a few and $\theta_{\rm e} \approx \theta_{\rm C}$. At larger radii the electron temperature $\theta_{\rm e}$ increases above the Compton temperature $\theta_{\rm C}$, as Comptonization gradually switches to the unsaturated regime with $y \approx k_{\rm h} + 2g/3$.

The region with $y \sim 1$ can extend over several expansion times. Therefore, the effective net Compton parameter can be substantially larger than unity and result in significant redistribution of photons, in particular above the spectral peak. The nonthermal high-energy tail is built in this regime, with an energy content comparable to that of the radiation near the peak. In addition to thermal Comptonization, the pair photon cascade initiated by the injected non-thermal leptons can extend the non-thermal tail to the GeV range.

The final low-energy slope of the photospheric spectrum is mainly formed at radii $r \gtrsim R_{\rm W}$, in the intermediate regime with $y \sim$ a few. It is shaped by the combination of photon Comptonization from low energies toward the peak, diffusion in energy space, and adiabatic cooling.

Some insight into the development of the low-energy slope is provided by the quasi-steady solution of the Comptonization problem at a given radius in the spectral range $E_0 < h\nu < k_{\rm B}T_{\rm e}$. The solution is found by setting the second term on the right side of Equation (3) to zero. Neglecting induced scattering, one finds[2]

$$I_\nu \propto {\rm C} + \nu^a e^{-h\nu/k_{\rm B}T_{\rm e}}, \tag{25}$$

where $C =$ const and $a = 3 - 4(3-g)/(3y)$. In the strongly saturated regime $y \gg 1$, the last term in Equation (25) gives the Wien spectrum with $a \approx 3$. The other term $I_\nu \propto \nu^0$ results from the steady photon flux in the energy space toward the Wien peak.

The relative amplitudes of the two components in I_ν depend on the generation rate of low-energy photons and the number of photons already accumulated in the Wien peak. As y decreases, the Wien peak becomes less pronounced relative to the $I_\nu \propto \nu^0$ component. The spectral hardening toward the peak becomes weaker, because a decreases from its saturated value. In addition, the peak itself is broadened by the competition between Comptonization and adiabatic cooling.

Our detailed numerical simulations confirm that the average spectrum approaches $I_\nu \propto \nu^0$ below the peak for a broad range of parameters. The most important requirement for this behavior is the existence of a low-energy photon source between $R_{\rm W}$ and $R_\star$. The spectrum $I_\nu \propto \nu^0$ corresponds to the photon index $\alpha = -1$, which coincides with the average photon index observed in GRBs (Kaneko et al. 2006).

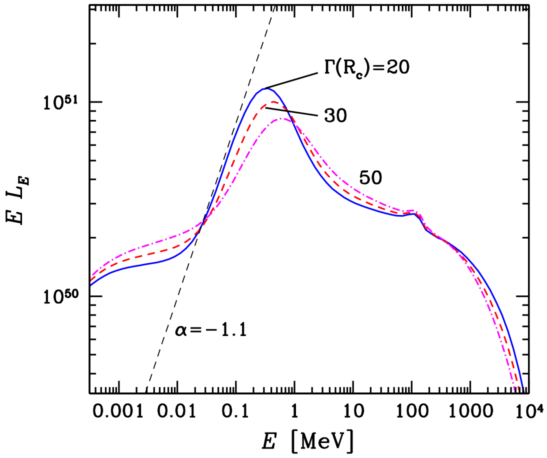

Figure 4. Effect of different Lorentz factors at $R_{\rm c}$ on the emitted spectrum. Other parameters are the same as in Figure 2.

3.5. *The role of the early acceleration stage and magnetization*

Figure 4 shows the response of the final (observed) spectrum to variations in the Lorentz factor at the collimation radius $\Gamma(R_{\rm c})$. Lowering Γ at $r < R_{\rm W}$ implies a higher density and increases the efficiency of photon production. In addition, $R_{\rm W}$ is increased, which increases the number of synchrotron photons reaching the spectral peak (see Equation C19). Both effects lead to a lower $E_{\rm pk}$.

The spectra become more narrow in jets that are still significantly accelerating between $R_{\rm W}$ and $R_\star$, i.e. those with a larger disparity between $\Gamma(R_{\rm c})$ and the final Γ. During the accelerating stage radiation carries a large fraction of the jet energy, which makes it less susceptible to spectral redistribution/broadening by dissipation. In addition, the ratio $R_\star/R_{\rm W}$ is smaller if the jet is still accelerating outside $R_{\rm W}$, leaving less time for broadening the spectrum.

Figure 5 shows the spectra for different jet magnetizations. With increasing $\varepsilon_{\rm B}$ the peak position shifts to lower energies, as more synchrotron photons are produced. This effect is partially offset by the suppression of pair loading (see Section 3.2 and V11), which reduces the Wien radius and the number of synchrotron-emitting particles.

The spectral shape exhibits a characteristic behavior as the magnetization is increased: more low-energy synchrotron photons tend to make the spectrum softer below the peak; a stronger low-energy "excess" is also produced. Above the peak the slope becomes steeper as synchrotron losses reduce IC emission from high-energy particles. Synchrotron losses also inhibit pair cascade, which

---

[2] The actual spectrum at a given r has time to relax to the steady state solution only if $y \gg 1$. When $y \sim$ a few, Equation (25) only shows the qualitative behavior of the spectrum, but does not give its exact shape.

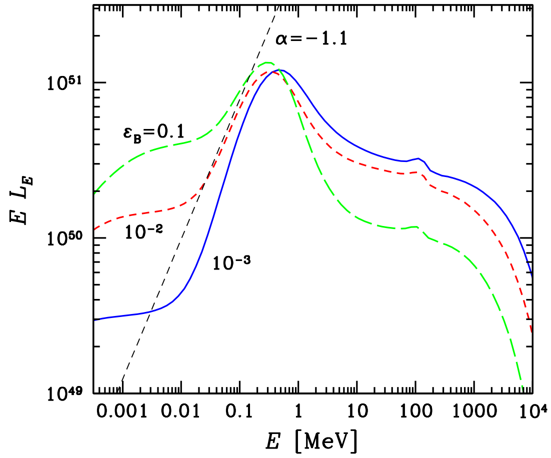

Figure 5. Effect of different magnetizations. Other parameters are the same as in Figure 2.

weakens and hardens the high-energy spectrum. As a result, the nonthermal IC emission creates a stronger upward curvature in the spectrum around 10 MeV.

4. FITS TO PROMPT GRB DATA

To test our transfer simulations against observations, we chose three bright GRBs with good spectral data and distinct spectral shapes: GRB 990123, GRB 090902B, and GRB 130427A. Good spectral fits were previously obtained with phenomenological models combining Band function (Band et al. 2009), a power law, and sometimes a Planck component. Our model will pass the test if it is able to reproduce the fits. Formal fitting utilizing an appropriate goodness of fit statistic as well as instrument response matrices is deferred to a future work.

The results are shown in Figures 6-8. The previous phenomenological fits are shown by red dashed curves (see Table 2 for fit parameters) and our transfer model is shown by solid blue curves. The achieved agreement demonstrates that the model is consistent with the data and provides estimates for the jet parameters for each GRB. The parameters are given in Table 1.

The transfer model also provides a physical interpretation for the previously suggested phenomenological components. In particular, the Band component below $\sim$ 10 MeV in all three bursts results from thermal Comptonization of low-energy photons by the heated plasma below the photosphere. The high-energy component from nonthermal Comptonization overlaps with the thermal Comptonization component and smoothly extends it beyond 10 MeV. The associated spectral hardening is more gradual if the thermal heating persists and dominates the dissipation above the photosphere, as in e.g. GRB 990123.

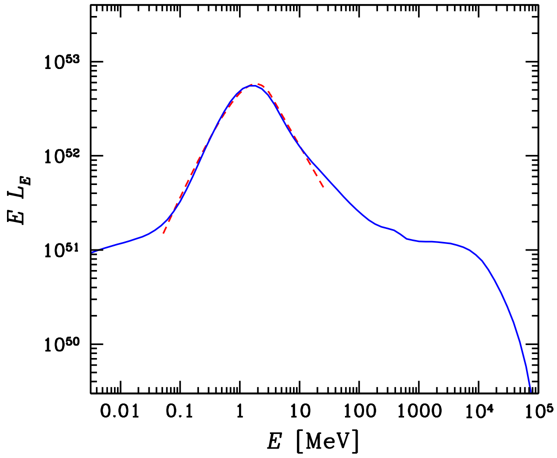

Figure 6. Simulated spectrum of GRB 990123 (solid line), and a Band fit (dashed line, Briggs et al. 1999). Jet parameters: Magnetization $\varepsilon_{\rm B} = 0.018$, simulations starting (collimation) radius $R_{\rm c} = 3\times10^{10}$ cm, initial Lorentz factor $\Gamma(R_{\rm c}) = 35$, initial number of photons per baryon $n_{\rm ph}(R_{\rm c})/n_{\rm p}(R_{\rm c}) = 5\times10^4$, terminal Lorentz factor $\Gamma_{\rm f} = 500$. The heating parameters are $\varepsilon_{0,\rm th} + \varepsilon_{0,\rm nth} = 0.26$, $\varepsilon_{0,\rm th}/\varepsilon_{0,\rm nth} = 4.7$, $k_{\rm th} = k_{\rm nth} = -0.19$. The heating proceeds until $\tau_{\rm T} = 0.01$.

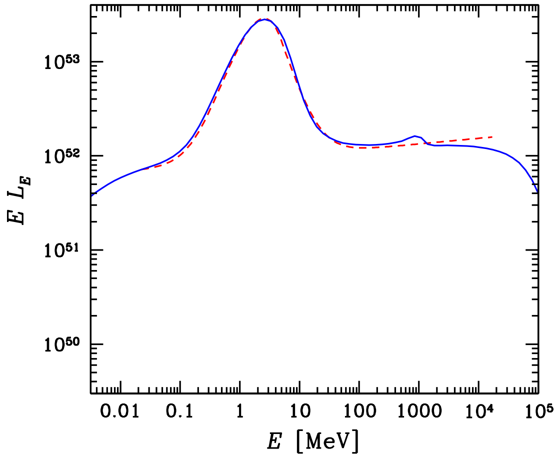

Figure 7. Simulated spectrum of GRB 090902B (solid line), and a Band+power-law fit (dashed line, Abdo et al. 2009, bin b). Jet parameters: $\varepsilon_{\rm B} = 0.012$, $R_{\rm c} = 3\times10^{10}$ cm, $\Gamma(R_{\rm c}) = 70$, $n_{\rm ph}(R_{\rm c})/n_{\rm p}(R_{\rm c}) = 10^5$, $\Gamma_{\rm f} = 1220$; Heating parameters $\varepsilon_{0,\rm th} + \varepsilon_{0,\rm nth} = 0.12$, $\varepsilon_{0,\rm th}/\varepsilon_{0,\rm nth} = 0.85$, $k_{\rm th} = k_{\rm nth} = -0.25$. The heating proceeds until $\tau_{\rm T} = 0.03$.

The case of GRB 090902B is particularly interesting, as it shows strong deviations from the Band function at both low and high energies. These deviations were previously modeled as an additional power law component that extends from the keV band up to GeV energies. Our transfer simulations show that the soft and hard excesses are produced by different radiative processes: synchrotron at low energies and IC at high energies. However, both are emitted by the same nonthermal $e^{\pm}$ population, a result of strong nonthermal heating of the jet around the photosphere. The simplest mechanism of nonthermal heating is the decay of pions produced by inelastic nuclear collisions (B10), which must operate in GRB jets unless they are strongly dominated by magnetic fields. We find that GRB 090902B has $\varepsilon_{\rm B} \approx 0.012$. This magnetization explains both the soft and hard excess. Remarkably, the same value of $\varepsilon_{\rm B}$ is required by the shape of the Band component observed in this burst.

Table 1
Jet parameters for the fitted GRBs.

GRB	L[a] $[10^{54}$ erg s$^{-1}]$	$\Gamma(R_c)$[b]	Γ_f[c]	η[d]	ϵ_B[e]	$\varepsilon_{0,h}$[f]	$\varepsilon_{0,th}/\varepsilon_{0,nth}$[g]	k_{th}[h]	k_{nth}[i]	$R_\star$[j] $[10^{13}$ cm$]$
990123	0.44	35	500	730	0.018	0.12	4.7	-0.19[k]	-0.19[k]	1
090902B	2.3	70	1220	1740	0.012	0.12	0.85	-0.25[l]	-0.25[l]	1
130427A	0.43	64	400	506	0.050	0.18	1.4	0.04[m]	$0.04 \to -2$[m]	2

[a] Total jet luminosity (isotropic equivalent).
[b] Jet Lorentz factor at R_c.
[c] Final Lorentz factor Γ_f achieved by the jet at large radii (calculated self-consistently from the model).
[d] Jet energy per unit rest mass η.
[e] Magnetization ε_B.
[f] Total heating rate $\varepsilon_{0,h} = \varepsilon_{0,th} + \varepsilon_{0,nth}$.
[g] Ratio of thermal to nonthermal heating $\varepsilon_{0,th}/\varepsilon_{0,nth}$.
[h] Radial scaling index of thermal dissipation k_{th}.
[i] Radial scaling index of nonthermal dissipation k_{nth}.
[j] Photospheric radius $R_\star$ (not a free parameter, calculated self-consistently from the model).
[k] Dissipation proceeds until $\tau_T = 0.01$.
[l] Dissipation proceeds until $\tau_T = 0.03$.
[m] The nonthermal dissipation law changes at $\tau_p = 30$. Dissipation proceeds until $\tau_T = 2$.

Table 2
Parameters of the phenomenological fits from the literature.

GRB	$E_{pk,obs}$[a] [keV]	α[b]	β[c]	Γ_{pl}[d]	$T - T_0$[e] [s]	Instrument	Reference
990123	720	-0.6	-3.11	-	12 – 45	*CGRO*/BATSE	Briggs et al. (1999)
090902B	908	0.07	-3.9	-1.94	4.6 – 9.6	*Fermi*	Abdo et al. (2009), bin b
130427A	1028	-0.958	-4.17	-	0 – 19	Konus/*Wind*	Golenetskii et al. (2013)

[a] Spectral peak position $E_{pk,obs}$ in the observer frame.
[b] Low-energy slope α.
[c] High-energy slope β.
[d] Power-law index in Band+PL fit.
[e] Time interval of the fitted data relative to the trigger.

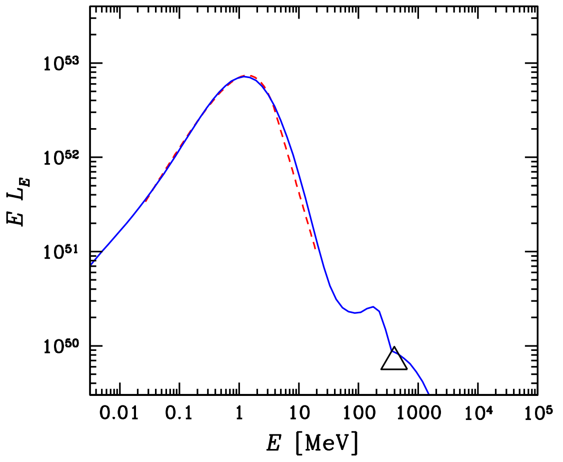

Figure 8. Simulated spectrum of GRB 130427A (solid line), and a Band fit (dashed line, Golenetskii et al. 2013). Jet parameters: $\varepsilon_B = 0.05$, $R_c = 3 \times 10^{11}$ cm, $\Gamma(R_c) = 64$, $n_{ph}(R_c)/n_p(R_c) = 1.2 \times 10^4$, $\Gamma_f = 400$; Heating parameters $\varepsilon_{0,th} + \varepsilon_{0,nth} = 0.18$, $\varepsilon_{0,th}/\varepsilon_{0,nth} = 1.4$, $k_{th} = k_{nth} = 0.04$; the non-thermal dissipation law changes into $k_{nth} = -2$ at $\tau_p = 30$, the heating proceeds until $\tau_T = 2$. The black triangle corresponds to the average flux above 100 MeV observed by *Fermi*/LAT during the most intense phase of the prompt emission (Ackermann et al. 2014).

The distinct spectral shapes in the three cases are mostly the result of different heating histories in the jet, as well as different partitioning of the dissipated energy between thermal and non-thermal channels. The absence of an extra component in GRB 990123 and GRB 130427A implies that non-thermal heating is weak in the optically thin parts of the jet. Furthermore, the steep, almost cutoff-like appearance of the spectrum above the peak in GRB 130427A suggests that most of the dissipation (thermal and nonthermal) is confined to regions below the photosphere, as heating at larger radii would tend to flatten the high-energy spectrum. This last point is quite general and can be applied to other bursts whose spectra have a cutoff power-law shape. In contrast, the relatively soft low-energy slope of GRB 130427A $\alpha \approx -1$ indicates that both dissipation channels have to be efficient at optical depths $\tau_T \gg 10$ below the photosphere, where the spectral slope α is formed. The softening of α is also helped by the strong magnetization $\varepsilon_B \approx 0.05$, which increases the supply of soft synchrotron photons.

Note that all three spectra peak just above 1 MeV, as is typical for bright GRBs. The transfer model naturally explains the peak position. It is regulated by the photon number in the Wien zone, which is calculated self-consistently with no fine tuning.

5. DISCUSSION

In this paper we studied the production of radiation by opaque, dissipative, relativistic jets. We used radiative transfer simulations to study the main features of the emission mechanism and to compare the theoretical spectra with observations. We presented a detailed physical model that fits the observed GRB spectra and thus allows us to measure the main parameters of the jet.

We used a somewhat simplified description of energy dissipation in the jet, with continual electron heating of two types, thermal and nonthermal. It is mainly motivated by the minimal heating model of B10 where electron/positron plasma receives energy from hot baryons through collisional processes, which are well defined and can be calculated from first principles. However, our simple parametrization of electron heating (power law scaling with radius, with a given slope and normalization) may also accommodate other heating models.

Another simplification adopted in this paper is the steady-state approximation to radiative transfer (see B11 for a discussion of this approximation). The theoretical spectra calculated in this work represent the average over the causal timescale near the photosphere $\delta t_\star \sim R_\star/\Gamma^2 c$, which is typically very short in the presented models, comparable to a few ms. The spectrum can evolve on timescales $\delta t > \delta t_\star$, as observed in GRBs. We believe that this evolution is controlled by the noisy process of jet formation and mass loading near the central engine, which is difficult to predict.

The main advantage of our transfer simulations is that they carefully include relevant radiative processes, so that the radiation spectrum is accurately calculated. Another advantage is that our dissipative jet model has a moderate number of parameters (seven for an unbroken dissipation profile and nine if a break is required by the data). Therefore, the transfer model can be used to fit observations. Unlike fits by phenomenological functions, fits by the physical model directly provide estimates for the main physical parameters of the GRB jets.

We find that a continuously heated and moderately magnetized jet naturally produces a Band-type spectrum, with spectral slopes α, β, and peak position $E_{\rm pk}$ consistent with observations. The bulk of the observed photons in a typical GRB do not originate from the central engine or the vicinity of the Thomson photosphere; instead they are produced in the opaque jet at optical depths $\tau_{\rm T} > 100$. The broadening of the spectrum into the final non-thermal shape takes place between $\tau_{\rm T} \sim 10$ and ~ 0.1.

A typical burst with $L \approx 10^{52}$ erg/s, a canonical Band spectrum, and $E_{\rm pk} \lesssim 1$ MeV is reproduced by the model if:

1. The jet magnetization is in the range $10^{-3} \lesssim \varepsilon_{\rm B} \lesssim 0.1$. Very weak magnetization increases $E_{\rm pk}$ by suppressing synchrotron emission; strong (near equipartition) magnetization softens the spectrum both below and above the peak, and generates a prominent soft "excess" below a few tens of keV.

2. The jet Lorentz factor $\Gamma(R_{\rm c}) \lesssim 100$ at radii comparable to that of the stellar progenitor. Low $E_{\rm pk}$ bursts are more "photon-rich" and require considerably lower $\Gamma(R_{\rm c})$ for more efficient photon production.

3. Heating has a nonthermal component that injects relativistic leptons into the jet. The absence of nonthermal leptons would lead to hard spectra with high $E_{\rm pk}$, due to the lack of synchrotron emission.

Our simulations demonstrate that nonthermal heating in the sub-photospheric region loads the jet with $e^\pm$ pairs via pair-photon cascades. In weakly magnetized jets the pairs outnumber protons by a factor comparable to 10, leading to the increase of the average photospheric radius by a similar factor. The jets remain forever dominated by $e^\pm$ pairs, which will affect afterglow emission produced by the reverse shock when the jet is decelerated by the external medium. The reverse shock emission might serve as a probe of pair loading.

5.1. *Spectral peak position*

Transfer simulations allow one to study the physical conditions in the jet, how the prompt radiation spectrum is formed, what controls the observed spectral index, the position of the peak etc.

The evolution of the radiation spectrum in the expanding jet takes place in two stages delineated by the Wien radius $R_{\rm W}$ where Comptonization switches from saturated to unsaturated regime. The photon number accumulated in the spectral peak and its observed position $E_{\rm pk}$ is determined near $R_{\rm W}$. Overall, we find that the dependence of $E_{\rm pk}$ on parameters is rather weak and no fine-tuning is necessary to bring the peak into the observed range around 1 MeV.

Note that in all models presented in this paper we chose the conservative assumption that the jet is initially photon starved — we chose a low initial photon number, which corresponds to a high initial $E_{\rm pk} \approx 10$ MeV. Then the exact initial condition is not important — it is quickly "forgotten" as many more photons are generated at larger radii. This assumption becomes inconsistent for relatively slow jets, which have a large Planck radius (B13, V13) or for fast jets with weak dissipation below the Wien radius. In these cases strong thermal radiation should be assumed at the inner boundary of the simulation.

The most efficient photon production mechanism, which controls the observed $E_{\rm pk}$ in our models, is synchrotron emission in the Wien zone $r < R_{\rm W}$, well inside the photopsheric radius $R_\star$. This mechanism works when a non-negligible fraction of the dissipated energy is channeled to nonthermal leptons. The constraints on jet magnetization in the photon production zone are less restrictive than suggested in V13 and Thompson & Gill (2014). We find that a moderate magnetization $\varepsilon_{\rm B} \gtrsim 10^{-3}$ is sufficient to generate the photon number observed in a typical GRB. V13 required $\varepsilon_{\rm B} \sim 1$ because they neglected pair cascades, which increase the number of synchrotron emitters, partially offsetting the reduction in synchrotron emissivity at small $\varepsilon_{\rm B}$. Also, the extended heating range considered in this work allows more time to accumulate photons in the Wien peak.

5.2. *Low energy slope α*

The typical photon index of observed GRB spectra at $E < E_{\rm pk}$ is $\alpha \sim -1$ (Kaneko et al. 2006). In the absence of synchrotron photon production, photospheric emission has a much harder spectrum (Pe'er et al. 2006; Giannios 2006; B10; V11), unless the jet has a very small collimation angle, comparable to Γ^{-1} (Lundman et al. 2013).

Our transfer simulations of magnetized jets with $\varepsilon_B > 10^{-3}$ naturally explain the observed $\alpha \sim -1$ and its variations (Figure 5). The softening of the low-energy slope begins near the Wien radius where the generated low-energy synchrotron photons are no longer Comptonized to the spectral peak, ending up at intermediate energies. For a broad range of parameters the resulting low-energy spectrum is roughly flat in number of photons per $\ln E$ (i.e. $\alpha = -1$). Similar low-energy slopes were recently obtained by Thompson & Gill (2014) in magnetically dominated jets. Despite the different regime, the spectrum formation below the peak is similar: unsaturated Comptonization of a low-energy photon source.

5.3. *Baryonic vs. Poynting-dominated jets*

In this work we have only considered moderately magnetized jets. Very weak magnetization $\varepsilon_B < 10^{-3}$ is disfavored based on the need for efficient photon generation and the observed spectral shape (in particular below the peak). On the other hand, our results do not exclude the possibility of a Poynting-dominated jet at small radii, as the initially dominant magnetic energy could have been dissipated at $r \ll R_\star$.

Radiation from magnetically dominated jets was recently considered by Thompson & Gill (2014), Gill & Thompson (2014) and Bégué & Pe'er (2015). Gill & Thompson envision a two-stage evolution of the jet beginning from a baryon-free Poynting flux followed by baryon loading and photospheric emission. In their picture, the opacity is due to electron-positron pairs generated by dissipation, which takes place in two separate episodes. The $e^\pm$ pairs also generate photons through cyclo-synchrotron emission. The evolution of radiative processes in their scenario resembles that in our jet models: the generation of synchrotron photons is followed by Comptonization into a Band-like spectrum.

5.4. *Models for individual bursts*

We applied our radiative transfer model to three well-studied bright bursts, GRB 990123, GRB 090902B, and GRB 130427A, which show different prompt spectra. Successful fits have been found in all three cases, giving estimates for the main parameters L, η, ε_B, $\Gamma(R_c)$, ε_{th}, and ε_{nth} (Table 1). In particular, we find the jet magnetizations $\varepsilon_B = 0.01 - 0.05$, and the Lorentz factors between 400 and 1200. The average photospheric radii $R_\star$ in the three bursts vary around 10^{13} cm.

These results suggest a systematic method for estimating the jet Lorentz factor in a larger sample of bursts, which is independent of another new method based on the reconstruction of the GeV+optical flash produced by the external blast wave at much larger radii $\gtrsim 10^{16}$ cm (Beloborodov et al. 2014; Vurm et al. 2014; Hascoët et al. 2015). For GRB 130427A we find $\Gamma_f = 400$, which within uncertainties is consistent with the value $\Gamma_{ej} = 350$ obtained from the GeV+optical flash reconstruction (Vurm et al. 2014). For GRB 090902B we find $\Gamma_f \approx 1200$, which is higher than $\Gamma_{ej} = 600 - 900$ used to fit the GeV flash (Hascoët et al. 2015). Note however that the reverse shock in GRB 090902B is relativistic; in this case there is a significant uncertainty in the upper limit on Γ_{ej} and the flash modeling only gives a lower limit $\Gamma_{ej} > 600$ (Hascoët et al. 2015).

In GRB 130427A we find that the nonthermal heating becomes weak well before the jet expands to transparency. Its nonthermal Band-like spectrum is mainly the result of thermal Comptonization. The weak residual high-energy emission from nonthermal heating still makes a significant contribution to the GeV luminosity and is consistent with the *Fermi* LAT data during the main prompt emission episode. It could also explain the variability superimposed on the smooth extended GeV flash in GRB 130427A.

The featureless Band spectrum of GRB 990123 suggests that thermal heating dominates the dissipation also in this burst. Our transfer model predicts a moderate excess below a few tens of keV due to synchrotron emission, similar but weaker than that observed in GRB 090902B. A hint of such excess is indeed seen in the data (Figure 2 in Briggs et al. 1999).

In contrast, nonthermal dissipation in GRB 090902B is strong up to the photosphere and beyond. It well explains the observed high-energy component and the soft excess, which were previously modeled as a power law of unknown origin (Abdo et al. 2009). The high-energy component is also expected to make a contribution to the GeV flash observed in GRB 090902B by *Fermi* LAT. Our result for the Lorentz factor $\Gamma \approx 1200$ is similar to the estimate by Pe'er et al. (2012). They used a different phenomenological model for GRB 090902B (a multicolor blackbody for the photosphere and nonthermal radiation from dissipation at a large radius) and estimated $\Gamma \approx 1000$.

Confining most of the dissipation to the subphotospheric region in bursts like GRB 130427A is expected if dissipation is caused by neutron-proton collisions, whose rate declines at $\tau_p \lesssim 20$ (B10). The heating of thermal electrons by Coulomb collisions with hot protons (stirred by n-p collisions) is also reduced at $\tau_\pm \ll m_p/(m_e \ln \Lambda)$, where $\ln \Lambda \sim 20$ is the Coulomb logarithm (Rossi et al. 2006; B10). Significant heating extending beyond the photosphere in GRB 090902B suggests the presence of a different dissipation mechanism. For instance, internal shocks can occur both below and above the photosphere, and the shocks can directly heat the photons and $e^\pm$ plasma without relying on n-p or Coulomb collisions (Beloborodov 2016).

Note that a systematic study of the entire parameter space was not attempted in this paper and is a currently ongoing work. Thus some degeneracies may be present between the parameters reported in Table 1, particularly if the actual dissipation profile is more complex than the "minimal" model used in this paper. The relatively featureless spectra of GRB 990123 and GRB 130427A are more prone to such degeneracies. In contrast, the prominent extra component(s) in GRB 090902B make this case more restrictive, thus the obtained solution and jet parameters are most likely unique.

5.5. *Future prospects*

Future analysis of GRB spectra using transfer simulations can be developed in two ways. (1) The transfer models give spectra that could be observed with a high temporal resolution $\delta t_\star \sim R_\star/\Gamma^2 c$, comparable to a few ms. The *evolving* nonthermal spectrum could be fitted by the model; it would show the evolution of the jet parameters during the burst. (2) Photon statistics in observed GRB spectra are usually accumulated on timescales $\delta t \gg \delta t_\star$, hindering the resolution of the instantaneous spectrum emitted by the variable jet. Then even the best time-resolved data analysis may give a mixture of different instantaneous spectra, which could result in the presence of multiple components in the measured spectrum. Transfer simulations may be used for the analysis of the multiple components. A dominant Band component is almost always found in GRBs, including the recent fits by the evolving mixture of three components: Band + power law + thermal (Guiriec et al. 2015). The nonthermal emission may be well explained by our model of a heated jet, including the excess at low and high energies which was previously viewed as a separate power law (see Figure 7). The model also predicts that emission from weakly heated jets has a quasi-thermal shape. Thus the presence of a quasi-thermal component (Ryde 2004, 2005; Ryde & Pe'er 2009; Guiriec et al. 2015) may indicate the presence of unresolved parts of the jet with weak heating.

The transfer model makes specific predictions for polarization of the prompt radiation (Lundman et al. 2016, in preparation), which can be tested by future observations. The polarized radiation arises from synchrotron emission by nonthermal electrons; it increases toward lower frequencies below the MeV peak and is strongest in the X-ray band. Bursts with strong nonthermal dissipation extending to the photosphere (such as GRB 090902B) will be most promising for the detection of polarization.

We thank Christoffer Lundman for helpful comments and discussions that helped to improve this manuscript. This work was supported by NSF grant AST-1412485 and NASA ATP grant NNX15AE26G.

APPENDIX

A. DISSIPATIVE JET DYNAMICS

Let us rewrite the radiative transfer equation (5) in the form

$$\frac{1}{r^2\Gamma^2}\frac{\partial}{\partial \ln r}\left[(1+\mu)r^2\Gamma^2 I_\nu\right] = \frac{r}{\Gamma}(j_\nu - \kappa_\nu I_\nu) + (1+\mu)(1-g)\, I_\nu + (1+\mu)(1-g\mu)\frac{\partial I_\nu}{\partial \ln \nu} - \frac{\partial}{\partial \mu}\left[(1-\mu^2)(1+\mu)\, g I_\nu\right]. \tag{A1}$$

Integrating Equation (A1) over the photon energy and taking the first two angular moments yields

$$\frac{1}{r^2\Gamma^2}\frac{d}{d\ln r}\left[r^2\Gamma^2(I_0+I_1)\right] = \frac{r}{\Gamma}(\bar{j} - \kappa I_0) - g(I_0 - I_2), \tag{A2}$$

$$\frac{1}{r^2\Gamma^2}\frac{d}{d\ln r}\left[r^2\Gamma^2(I_1+I_2)\right] = -\frac{r}{\Gamma}\,\kappa I_1 + g(I_0 - I_2), \tag{A3}$$

where $\bar{j}$ is the angle-averaged bolometric emissivity and we have assumed an isotropic (comoving) opacity κ. The moments of intensity I_1, I_2 and I_3 are defined as

$$I_m = \frac{1}{2}\int d\nu \int_{-1}^{1} I_\nu(\mu)\, \mu^m\, d\mu. \tag{A4}$$

The lab frame luminosity is given by $L_{\rm rad} = (4\pi)^2 r^2\Gamma^2(I_0 + 2I_1 + I_2)$ (using $\Gamma \gg 1$, see B11). The equation governing its evolution is obtained by adding Equations (A2) and (A3),

$$\frac{dL_{\rm rad}}{d\ln r} = (4\pi)^2 r^3 \Gamma\left[\bar{j} - \kappa(I_0 + I_1)\right]. \tag{A5}$$

The dissipation rate in the comoving frame is $dE_{\rm h}/(dV'dt') = 4\pi(\bar{j} - \kappa I_0)$. Transformation to the lab frame yields

$$\frac{dL_{\rm h}}{d\ln r} = 4\pi r^3\Gamma\frac{dE_{\rm h}}{dV'dt'} = (4\pi)^2 r^3\Gamma\,(\bar{j} - \kappa I_0). \tag{A6}$$

Equation (A5) thus becomes

$$\frac{dL_{\rm rad}}{d\ln r} = \frac{dL_{\rm h}}{d\ln r} - (4\pi)^2 r^3\Gamma\,\kappa I_1. \tag{A7}$$

The second term on the right hand side describes the work done by the radiation field on accelerating the jet.

If dissipation is described as redistribution of the total energy $L = L_{\rm pl} + L_{\rm rad} = {\rm const}$ from the bulk kinetic ($L_{\rm pl}$) to internal (radiation-dominated) form, one can write $L_{\rm rad} = L(1 - \Gamma/\eta)$ to obtain a dynamical equation for the jet Lorentz factor

$$\frac{d\Gamma}{dr} = -\eta\frac{d\varepsilon_{\rm h}}{dr} + \sigma_{\rm T} Z_\pm \frac{4\pi I_1}{m_p c^3}, \tag{A8}$$

where $d\varepsilon_{\rm h}/d\ln r = L^{-1}dL_{\rm h}/d\ln r$. Alternatively, the heat source can be modelled as a "reservoir" of free energy carried by the jet in the form of internal bulk motions, $L_{\rm turb}$. Then $L = L_{\rm pl} + L_{\rm rad} + L_{\rm turb} = {\rm const}$, and the energy balance is given by

$$\frac{dL_{\rm h}}{d\ln r} = \frac{dL_{\rm rad}}{d\ln r} + \dot{M}c^2\frac{d\Gamma}{d\ln r}. \tag{A9}$$

In this case, the dynamical equation becomes

$$\frac{d\Gamma}{dr} = \sigma_{\rm T}Z_\pm\frac{4\pi I_1}{m_pc^3}. \tag{A10}$$

In the optically thick domain it is useful to rewrite the dynamical equation in a form where the (small) first moment I_1 of the intensity does not appear. In such case $I_2 \approx I_0/3 \gg I_1$ and $L_{\rm rad} = (4/3)(4\pi)^2r^2\Gamma^2I_0$, whereby Equation (A2) can be written as

$$\frac{dL_{\rm rad}}{d\ln r} = \frac{4}{3}\frac{dL_{\rm h}}{d\ln r} - \frac{2g}{3}L_{\rm rad}, \tag{A11}$$

where the last term accounts for adiabatic cooling. In place of Equation (A8) one now obtains

$$\frac{d\ln\Gamma}{d\ln r} = \frac{1}{2+\Gamma/\eta}\left[2\left(1-\frac{\Gamma}{\eta}\right) - 4\frac{d\varepsilon_{\rm h}}{d\ln r}\right]. \tag{A12}$$

In the absence of dissipation Equation (A12) can be integrated straightforwardly to yield the standard solution for Γ in baryonic (initially) radiation dominated jets (see e.g. Piran et al. 1993).

In the reservoir model of the heat source Equation (A10) is replaced by

$$\frac{d\ln\Gamma}{d\ln r} = \frac{2L_{\rm rad} - dL_{\rm h}/d\ln r}{3\Gamma\dot{M}c^2 + 2L_{\rm rad}}. \tag{A13}$$

B. PAIR-LOADING IN A DISSIPATIVE JET

The cooling of the injected $e^\pm$ pairs and their subsequent thermalization is very efficient in the high compactness environment of GRB jets. Thus bulk of the $e^\pm$ pairs reside in a Maxwellian distribution at any given time. Their density is controlled by injection of new pairs (both primary particles as well as secondaries from the cascade), $e^\pm$ annihilation, and expansion of the jet (cf. B10),

$$\frac{c}{r^2}\frac{d}{dr}\left(\Gamma r^2 n_\pm\right) = \dot{n}_\pm - \dot{n}_{\rm ann}, \tag{B1}$$

where

$$\dot{n}_\pm = \frac{Y\varepsilon_{\rm nth}L}{4\pi m_{\rm e}c^2r^3\Gamma}, \qquad \dot{n}_{\rm ann} = \frac{3}{4}c\sigma_{\rm T}\,n_+n_- = \frac{3}{16}c\sigma_{\rm T}\,(n_\pm^2 - n_{\rm p}^2), \tag{B2}$$

and $n_\pm = n_+ + n_- = 2n_+ + n_{\rm p}$. The pair yield Y characterizes the fraction of energy injected into the primary pairs that ends up in pair rest mass through the pair-photon cascade. Defining the pair loading $Z_\pm = n_\pm/n_{\rm p}$, and using $\Gamma r^2 n_{\rm p} = \dot{M}/(4\pi m_{\rm p}c) = {\rm constant}$, Equation (B1) can be written as

$$\frac{dZ_\pm}{d\ln r} = \frac{Y\varepsilon_{\rm nth}L}{\Gamma\dot{M}c^2}\frac{m_{\rm p}}{m_{\rm e}} - \frac{3}{16}\tau_{\rm p}(Z_\pm^2 - 1), \tag{B3}$$

where $\tau_{\rm p} = \sigma_{\rm T}n_{\rm p}r/\Gamma$.

Two regimes can be identified in Equation (B3): (1) creation-annihilation balance, where both terms on the RHS are larger than the LHS, and (2) freezeout, where annihilation (last term) is negligible. In creation-annihilation balance the pair loading evolves as

$$Z_\pm = \left(\frac{16Y\varepsilon_{\rm nth}L}{3\tau_{\rm p}\,\Gamma\dot{M}c^2}\frac{m_{\rm p}}{m_{\rm e}} + 1\right)^{1/2}. \tag{B4}$$

Annihilation freezes out once $\tau_\pm = Z_\pm\tau_{\rm p} = 16/3$; beyond this radius the pair loading is governed by the first two terms in Equation (B3) and can increase at most by a logarithmic factor in radius (assuming a logarithmically flat heating rate and $\Gamma = {\rm const}$).

C. PHOTON PRODUCTION BY SYNCHROTRON EMISSION

The rate at which photons are generated and accumulated in the spectral peak depends on the interplay between synchrotron emission, reabsorption, IC scattering and induced Compton downscattering. It was shown in V13 that competition between these processes defines a characteristic photon energy above which the emitted synchrotron photons are upscattered to the Wien peak rather than downscattered and/or reabsorbed. Below we extend the results of V13 to include pair-photon cascades and apply them to the extended heated Wien zone.

At high optical depths the timescales for all relevant radiative processes are much shorter than the jet expansion timescale. In this regime the Kompaneets equation can be written as

$$-\frac{\sigma_T n_{\rm e}}{m_e c}\frac{1}{E^2}\frac{\partial}{\partial E}E^4\left(k_{\rm B}T_{\rm e}\frac{\partial \tilde{n}}{\partial E}+\tilde{n}^2\right)=\tilde{j}_\nu(E)-c\,\kappa(E)\tilde{n}, \tag{C1}$$

where $\tilde{n}$ is the photon occupation number, $\tilde{j}_\nu$ is the emissivity (here we consider only synchrotron) in units of the number of photons per unit phase space volume per second, κ is the (synchrotron absorption) opacity, $n_{\rm e}$ is the density of the thermal electron/positron component, and $T_{\rm e}$ is the electron temperature. We have neglected the recoil term in Equation (C1) since photon generation takes place at $E \ll k_{\rm B}T_{\rm e} \ll m_{\rm e}c^2$ where recoil losses are negligible.

By comparing the terms in Equation (C1) one can identify three regimes where different physical processes dominate. At low enough photon energies the radiation has the usual optically thick synchrotron spectrum for power-law electrons,[3]

$$\tilde{n}=\frac{\tilde{j}_\nu}{c\kappa}=\frac{1}{p+2}\left(\frac{E}{E_{\rm B}}\right)^{1/2}\left(\frac{E}{m_{\rm e}c^2}\right)^{-1}. \tag{C2}$$

As the synchrotron emitting electrons are relativistic, the brightness temperature of the optically thick synchrotron radiation $T_{\rm B} \equiv E\tilde{n}/k_{\rm B} \gg T_{\rm e}$. In this case the induced scattering term dominates the Kompaneets operator, tending to downscatter the synchrotron photons. The first break in the spectrum occurs where the induced scattering rate becomes dominant over the reabsorption rate. Above this energy (but before the second break, see below) the Kompaneets equation reduces to

$$-\frac{\sigma_T n_{\rm e}}{m_e c}\frac{1}{E^2}\frac{\partial}{\partial E}E^4\tilde{n}^2=\tilde{j}_\nu(E). \tag{C3}$$

The synchrotron emissivity of a power-law distribution of electrons, $n_{\rm e}(\gamma)=n_0\gamma^{-p}$, is

$$\tilde{j}_\nu(E)=j_0\left(\frac{E}{E_{\rm B}}\right)^{-(p+5)/2}=\frac{\pi}{4}\alpha_{\rm f}^{-1}c\sigma_{\rm T}n_0\left(\frac{m_{\rm e}c^2}{E_{\rm B}}\right)^2\left(\frac{E}{E_{\rm B}}\right)^{-(p+5)/2}, \tag{C4}$$

where $\alpha_{\rm f}=e^2/\hbar c$ if the fine structure constant and $E_{\rm B}=\hbar\,eB/m_e c$. The solution of Equation (C3) takes the form

$$\tilde{n}=\left[\frac{2m_e c\,\tilde{j}_\nu(E)}{(p-1)\sigma_{\rm T}n_{\rm e}E}\right]^{1/2}\propto E^{-(p+7)/4}. \tag{C5}$$

Compton upscattering begins where the radiation brightness temperature decreases down to the electron temperature. This yields the second break in the spectrum, above which the usual thermal Comptonization spectrum is established. The characteristic energy, E_0, can be found by equating the two terms in the Comptonization operator in Equation (C1),

$$-k_{\rm B}T_{\rm e}\frac{\partial \tilde{n}}{\partial E}=\tilde{n}^2. \tag{C6}$$

Using the spectrum (C5), this yields

$$\frac{p+7}{4}\,\frac{k_{\rm B}T_{\rm e}}{E_0}=\tilde{n}(E_0), \tag{C7}$$

or equivalently

$$\frac{(p-1)(p+7)^2}{32}\,\frac{(k_{\rm B}T_{\rm e})^2}{E_0}\,\frac{\sigma_{\rm T}n_{\rm e}}{m_{\rm e}c}=\tilde{j}_\nu(E_0). \tag{C8}$$

To proceed, one has to specify the electron distribution. Let us assume that relativistic electrons are continuously injected at a fixed Lorentz factor $\gamma_{\rm inj}$ with power $Q_{\rm inj}$ [$\rm erg\cdot cm^{-3}\cdot s^{-1}$]. The injected high-energy pairs initiate a pair-photon cascade with a large number of secondaries. Let us denote their number per injected primary particle as $\mathcal{M}_{\rm s}$. Denoting the pair yield as $Y=\mathcal{M}_{\rm s}/\gamma_{\rm inj}$ we can express the equilibrium pair distribution in the cascade as

$$n_{\rm e}(\gamma)=n_0\gamma^{-p}, \tag{C9}$$

---

[3] Here we are using the delta-function approximation, assuming that all synchrotron photons from a single electron are emitted at $E=0.3\gamma^2E_{\rm B}$.

where

$$n_0 = \frac{3Y\gamma_{\pm,\min}^{\alpha_\pm}}{4c\sigma_{\rm T}} \frac{\varepsilon_{\rm nth}}{(\varepsilon_{\rm B}+\varepsilon_{\rm rad})} \frac{c\Gamma}{r}, \tag{C10}$$

$p = 2 + \alpha_\pm$, $\gamma_{\pm,\min}$ is the electron energy below which the saturated cascade turns off, and $\alpha_\pm \approx \ln \mathcal{M}_{\rm s}/(\ln\gamma_{\rm inj} - \ln\gamma_{\pm,\min})$. The energy fractions $\varepsilon_{\rm B}$ and $\varepsilon_{\rm rad}$ are defined via

$$U_{\rm B} = \frac{\varepsilon_{\rm B} L}{4\pi c r^2\Gamma^2} \quad \text{and} \quad U_{\rm rad} = \frac{\varepsilon_{\rm rad} L}{4\pi c r^2 \Gamma^2}, \tag{C11}$$

and $\varepsilon_{\rm nth}$ is the fraction of total available energy deposited into the injected electrons per logarithmic radius interval,

$$\varepsilon_{\rm nth} L = \frac{dL_{\rm nth}}{d\ln r} = 4\pi r^3 \Gamma Q_{\rm inj}. \tag{C12}$$

Using n_0 given by Equation (C10) in the expression (C4) for the emissivity and inserting the latter into (C8) yields the critical photon energy/electron Lorentz factor

$$\left(\frac{E_0}{E_{\rm B}}\right)^{(p+3)/2} = (\sqrt{0.3}\,\gamma_0)^{p+3} = \frac{96\pi}{(p-1)(p+7)^2}\alpha_{\rm f}^{-1} \frac{\varepsilon_{\rm nth}\, Y\gamma_{\pm,\min}^{\alpha_\pm}}{(\varepsilon_{\rm B}+\varepsilon_{\rm rad})} \frac{\tau_{\rm T}}{y^2} \left(\frac{E_{\rm B}}{m_{\rm e}c^2}\right)^{-1}. \tag{C13}$$

Here $\tau_{\rm T} = \sigma_{\rm T} Z_\pm n_{\rm p} r/\Gamma$, $y = 4\tau_{\rm T}\theta_{\rm e}$ is the Compton parameter and the baryon number density is given by

$$n_{\rm p} = \frac{L}{4\pi m_{\rm p} c^3 r^2 \Gamma\eta}. \tag{C14}$$

The value of the critical Lorentz factor γ_0 is typically between a few and a few tens. If the pair cascades are suppressed (e.g. by synchrotron cooling), one obtains

$$\gamma_0 = 7.8\, L_{52}^{-3/10}\, R_{10}^{2/5}\, \Gamma_1^{3/5}\, \eta_3^{1/5}\, \gamma_{\rm inj,2}^{-1/5}\, \theta_{-2}^{-2/5}\, \varepsilon_{\rm B}^{-1/10} \left(\frac{\varepsilon_{\rm nth}}{\varepsilon_{\rm B}+\varepsilon_{\rm rad}}\right)^{1/5}. \tag{C15}$$

The synchrotron photon production rate at $E > E_0$ is

$$\dot{\mathcal{N}}_{\rm synch} = \frac{4\pi}{(ch)^3}\int_{E_0} \tilde{j}_\nu(E) E^2\, dE = \frac{3}{2(p-1)} \frac{\varepsilon_{\rm nth} Y\gamma_{\pm,\min}^{\alpha_\pm}}{(\varepsilon_{\rm B}+\varepsilon_{\rm rad})} \frac{c\Gamma}{r} \frac{U_{\rm B}}{E_{\rm B}} \left(\frac{E_0}{E_{\rm B}}\right)^{-(p-1)/2}. \tag{C16}$$

At a sphere of radius r, the number flux of photons produced between $r_{\min}$ and r is

$$\dot{N}_{\rm ph}(r) = \int_{r_{\min}}^{r} 4\pi r^3\, \dot{\mathcal{N}}_{\rm synch}(r)\, d\ln r. \tag{C17}$$

The quantities $\varepsilon_{\rm rad}(r)$ and $\Gamma(r)$ are determined by the heating model, in particular by $dL_{\rm h}/d\ln r$, see Equations (A11) and (A13). One last quantity entering the photon production rate is the electron temperature. In the Wien zone it can be determined from the relation

$$L_{\rm rad} = \frac{4}{3}\varepsilon_{\rm rad} L = 4\Gamma k_{\rm B} T_{\rm e}\, \dot{N}_{\rm ph}. \tag{C18}$$

For given cascade parameters Y and $\gamma_{\pm,\min}$, Equations (C13) – (C18) along with (A11) and (A13) form a closed set. Its solution gives the number of synchrotron photons $\dot{N}_{\rm ph}(r)$ which are Comptonized toward the Wien peak. The solution is simplified if one uses the approximation $\dot{N}_{\rm ph} \approx 4\pi r^3\, \dot{\mathcal{N}}_{\rm synch}$.

It is convenient to express the result as the number of produced photons per proton, $n_{\rm ph}/n_{\rm p} = \dot{N}_{\rm ph}/\dot{N}_{\rm p}$, where $\dot{N}_{\rm p} = L/(m_{\rm p}c^2\eta)$ is the proton number flux carried by the flow. In the absence of $e^\pm$ cascade, $\alpha_\pm = 0$ and $Y = \gamma_{\rm inj}^{-1}$, one finds

$$\frac{n_{\rm ph}}{n_p} = 4.1\times 10^6\, L_{52}^{-1/7}\, r_{10}^{3/7}\, \Gamma_1^{-5/7}\, \eta_3^{6/7}\, \gamma_{\rm inj,2}^{-4/7}\, \varepsilon_{\rm B}^{3/7}\, \varepsilon_{\rm rad}^{2/7} \left(\frac{\varepsilon_{\rm nth}}{\varepsilon_{\rm B}+\varepsilon_{\rm rad}}\right)^{4/7}. \tag{C19}$$

In the opposite limit of a fully saturated cascade one obtains

$$\frac{n_{\rm ph}}{n_p} = 1.83\times 10^7\, r_{10}^{1/5}\, \Gamma_1^{-1}\, Z_\pm^{1/5} \eta_3^{4/5} \varepsilon_{\rm B}^{2/5}\, \varepsilon_{\rm rad}^{2/5} \left(\frac{\varepsilon_{\rm nth}}{\varepsilon_{\rm B}+\varepsilon_{\rm rad}}\right)^{2/5}, \tag{C20}$$

where we used $p = 3$ ($\alpha_\pm = 1$). In a general case, the radial dependence of photon production is given by

$$\frac{n_{\rm ph}}{n_p} \propto r^{\frac{5-p}{3p+1}}\,\Gamma^{\frac{-5p+5}{3p+1}}\,Z_\pm^{\frac{p-1}{3p+1}}\,\varepsilon_{\rm rad}^{\frac{2p-2}{3p+1}}\left(\frac{\varepsilon_{\rm nth}Y\gamma_{\pm,\rm min}^{\alpha_\pm}}{\varepsilon_{\rm B}+\varepsilon_{\rm rad}}\right)^{\frac{4}{3p+1}}. \tag{C21}$$

The above analysis neglects some effects that are not straightforward to describe analytically. In particular, near the critical Lorentz factor $\gamma_0 \sim 10$, the IC cooling is modified by the Klein-Nishina effect, as the target photon energy in the electron rest frame $\sim 3k_{\rm B}T_{\rm e}\gamma_0$ is comparable to $m_{\rm e}c^2$. The Klein-Nishina recoil effect also influences the fate of the IC photons — they can scatter and lose energy to electron recoil before annihilating into pairs. This effect is particularly important for those IC photons that see a low opacity for pair production, which happens if they are below the threshold for interacting with the Wien-peak radiation. These effects can substantially alter the number of electrons near γ_0, and consequently the number of produced synchrotron photons. The above analytic estimates can only serve as a rough guide to the photon production showing its trends, i.e. the dependence on r, $\varepsilon_{\rm B}$, Γ etc. The accurate photon number is provided by our numerical simulations.

REFERENCES

Abdo, A. A., Ackermann, M., Ajello, M., et al. 2009, ApJ, 706, L138
Ackermann, M., Ajello, M., Asano, K., et al. 2014, Science, 343, 42
Axelsson, M., & Borgonovo, L. 2015, MNRAS, 447, 3150
Band, D., Matteson, J., Ford, L., et al. 1993, ApJ, 413, 281
Band, D. L., Axelsson, M., Baldini, L., et al. 2009, ApJ, 701, 1673
Baring, M. G., & Braby, M. L. 2004, ApJ, 613, 460
Bégué, D., & Pe'er, A. 2015, ApJ, 802, 134
Beloborodov, A. M. 2010, MNRAS, 407, 1033
—. 2011, ApJ, 737, 68
—. 2013, ApJ, 764, 157
—. 2016, submitted to ApJ (arXiv:1604.02794)
Beloborodov, A. M., Hascoët, R., & Vurm, I. 2014, ApJ, 788, 36
Beloborodov, A. M., Stern, B. E., & Svensson, R. 2000, ApJ, 535, 158
Briggs, M. S., Band, D. L., Kippen, R. M., et al. 1999, ApJ, 524, 82
Burgess, J. M., Preece, R. D., Baring, M. G., et al. 2011, ApJ, 741, 24
Burgess, J. M., Preece, R. D., Connaughton, V., et al. 2014, ApJ, 784, 17
Drenkhahn, G., & Spruit, H. C. 2002, A&A, 391, 1141
Eichler, D., & Levinson, A. 2000, ApJ, 529, 146
Giannios, D. 2006, A&A, 457, 763
—. 2008, A&A, 480, 305
Giannios, D., & Spruit, H. C. 2007, A&A, 469, 1
Gill, R., & Thompson, C. 2014, ApJ, 796, 81
Goldstein, A., Burgess, J. M., Preece, R. D., et al. 2012, ApJS, 199, 19
Golenetskii, S., Aptekar, R., Frederiks, D., et al. 2013, GRB Coordinates Network, 14487, 1
Guiriec, S., Kouveliotou, C., Daigne, F., et al. 2015, ApJ, 807, 148
Hascoët, R., Vurm, I., & Beloborodov, A. M. 2015, ApJ, 813, 63
Kagan, D., Sironi, L., Cerutti, B., & Giannios, D. 2015, Space Sci. Rev.
Kaneko, Y., Preece, R. D., Briggs, M. S., et al. 2006, ApJS, 166, 298
Lazzati, D., Morsony, B. J., & Begelman, M. C. 2009, ApJ, 700, L47
Levinson, A. 2012, ApJ, 756, 174
Lundman, C., Pe'er, A., & Ryde, F. 2013, MNRAS, 428, 2430
Mészáros, P., & Rees, M. J. 2000, ApJ, 530, 292
Mihalas, D. 1980, ApJ, 237, 574
Morsony, B. J., Lazzati, D., & Begelman, M. C. 2010, ApJ, 723, 267
Pe'er, A., Mészáros, P., & Rees, M. J. 2006, ApJ, 642, 995
Pe'er, A., & Ryde, F. 2011, ApJ, 732, 49
Pe'er, A., Zhang, B.-B., Ryde, F., et al. 2012, MNRAS, 420, 468
Piran, T., Shemi, A., & Narayan, R. 1993, MNRAS, 263, 861
Preece, R., Burgess, J. M., von Kienlin, A., et al. 2014, Science, 343, 51
Preece, R. D., Briggs, M. S., Mallozzi, R. S., et al. 2000, ApJS, 126, 19
Rees, M. J., & Meszaros, P. 1994, ApJ, 430, L93
Rossi, E. M., Beloborodov, A. M., & Rees, M. J. 2006, MNRAS, 369, 1797
Ryde, F. 2004, ApJ, 614, 827
—. 2005, ApJ, 625, L95
Ryde, F., & Pe'er, A. 2009, ApJ, 702, 1211
Ryde, F., Pe'er, A., Nymark, T., et al. 2011, MNRAS, 415, 3693
Sironi, L., & Spitkovsky, A. 2011, ApJ, 726, 75
Svensson, R. 1987, MNRAS, 227, 403
Thompson, C. 1994, MNRAS, 270, 480
Thompson, C., & Gill, R. 2014, ApJ, 791, 46
Thompson, C., Mészáros, P., & Rees, M. J. 2007, ApJ, 666, 1012
Vurm, I., Beloborodov, A. M., & Poutanen, J. 2011, ApJ, 738, 77
Vurm, I., Hascoët, R., & Beloborodov, A. M. 2014, ApJ, 789, L37
Vurm, I., Lyubarsky, Y., & Piran, T. 2013, ApJ, 764, 143

Vurm, I., & Poutanen, J. 2009, ApJ, 698, 293
Yu, H.-F., van Eerten, H. J., Greiner, J., et al. 2015, A&A, 583, A129